

Deep Mapper Graph and its Application to Visualize Plausible Pathways on High-Dimensional Distribution with Small Time-Complexity

Ziyad Oulhaj^{a,1}, Yoshiyuki Ishii^b, Kento Ohga^b, Kimihiro Yamazaki^b, Mutsuyo Wada^b, Yuhei Umeda^b, Takashi Kato^b, Yuichiro Wada^{b,c}, Hiroaki Kurihara^{b,*}

^aNantes Université, École Centrale Nantes, CNRS, Laboratoire de Mathématiques Jean Leray, UMR 6629, 2 Chemin de la Houssinière, Nantes, F-44000, France

^bFujitsu Limited, 4-1-1 Kamikodanaka, Nakahara-ku, Kawasaki-shi, Kanagawa, 211-8588, Japan

^cRIKEN AIP, Nihonbashi 1-chome Mitsui Building, 15th floor, 1-4-1 Nihonbashi, Chuo-ku., Tokyo, 103-0027, Japan

Abstract

Mapper is a topology based data analysis method that extracts topological features from high-dimensional data. The Mapper algorithm requires a filter function that maps the dataset to a Euclidian space and a clustering method, that is performed on the original dataset. This produces a graph which represents the shape of the original data. In this work, we use Mapper to uncover the conformational change of protein structures and we choose the filter function from a parameterized family, based on a deep neural network architecture. By optimizing its parameters with respect to an Energy-loss function derived from a theoretical background, we produce a Mapper graph that unveils the conformational pathways undertaken by the studied protein. Our method tackles conformational pathway detection in a unsupervised manner and therefore greatly reduces the manual and time costs necessary in this task.

Keywords: Mapper Graph, Topological Data Analysis, Deep Learning, Conformational Pathway, Protein Pathway, Cryo-EM

1. Introduction

Acquiring a summary of plausible paths (a.k.a. ridgelines) on a high-dimensional distribution is beneficial in several domains such as food and drug discovery. In those domains, acquiring plausible conformational paths with chemical structural change can enhance the efficiency for creating a new product.

Despite the demands, there only exists methods to compute one plausible path with long running time, i.e., there exists no method to summarize such paths with short running

*Corresponding author

Email address: h_kurihara@fujitsu.com (Hiroaki Kurihara)

¹This was a joint-work with Fujitsu, and the mentor was H. Kurihara.

time, to the best of our knowledge. The example methods to compute one plausible path are Barroso da Silva et al. (2020); Wu et al. (2022); Kinman et al. (2023).

As a brief review of aforementioned references, in food domain, a combined method of Molecular Dynamics (MD) and Quantitative Structure-Activity Relationships (QSARs) can assist in constructing a plausible conformational path (Barroso da Silva et al., 2020), where QSARs is an approach that predicts principles by correlating physico-chemical properties with biological properties. The conformational path leads to the elucidation of mechanisms such as pH-controlled immobilization and taste receptors. However, the method is based on MD, and therefore it takes a long time to compute a plausible conformational path.

In drug discovery, a protocol by Kinman et al. (2023) guides the construction of a plausible path with a protein structural change, utilizing an auto-encoder named cryo-DRGN (Zhong et al., 2021). Here, the structure is not expressed by an all-atom model of MD but a 3D density map, and the path is represented by a sequence of 3D density maps. In addition, cryoDRGN is trained by a set of 2D projection protein images collected by cryo-Electron Microscopy (cryo-EM) (Earl et al., 2017), and a trained cryoDRGN predicts the corresponding protein 3D density map from a latent variable. According to Kinman et al. (2023), it takes 2 to 3 days to compute one plausible path, since the pathway needs to be carefully constructed from latent variables with manual labor and extra biological tools. This implies that it takes much longer time to acquire a summary of multiple plausible paths, if we naively use the protocol.

In recent years, Kato et al. (2020) have proposed an auto-encoder named RaDOGAGA which can construct an isometric latent space to the original space, taking advantage of manifold assumptions (Chapelle et al., 2010). Thereafter, based on RaDOGAGA, Yamazaki et al. (2023) have proposed an auto-encoder called cryoTWIN that can construct an isometric latent space to a space of 3D density maps. Similar to cryoDRGN, cryoTWIN is trained on a set of cryo-EM images. In the numerical experiments in Yamazaki et al. (2023), using the isometric space, the authors computed a plausible conformational path of 50S-ribosomal dataset² with much shorter running time than Kinman et al. (2023).

However, in our preliminary experiments, we still take several hours to acquire a summary of the plausible protein pathways, since many random samples in the latent space are generated to construct one pathway in Algorithm 1 in Yamazaki et al. (2023). We describe details of the preliminary experiments in Section 2.1.3.

Considering the background above, our goal of this study is to propose a method to visualize a summary of plausible paths on a high-dimensional distribution with short running time, utilizing an isometric latent space introduced by an auto-encoder such as cryoTWIN. To achieve this goal, we focus on the mapper algorithm, which outputs a graph called a Mapper graph. It takes a set of points and a continuous real valued function, called a filter function, defined on those points as input, as well as other parameters. The

²The authors in Zhong et al. (2020) publicly share this dataset with the estimated pose orientation by cryoSPARC.

graph constitutes a visualization of the topological structure (loops, branches, connected components) of the data. The algorithm usually handles datasets with several tens of dimension, and the running time to return the graph is sufficiently short. Although there exists a wide range of applications of the mapper algorithm, the choice of the filter function has hindered many of them, since summarizing complex data structure can suffer from using naive filter functions. Then, in order to answer the problem, Oulhaj et al. (2024) have proposed a mapper algorithm, where the filter function is parameterized, and the function is optimized to output a well-summarized mapper graph for the complex data structure, based on a topological criteria.

We summarize our contributions in this study, as follows:

1. Inspired by Oulhaj et al. (2024), we propose a generic mapper algorithm, whose filter function is parameterized by a deep neural network. This generic algorithm returns a visualized summary of plausible paths on a high-dimensional distribution, based on a method introducing a low-dimensional isometric space such as cryoTWIN (Yamazaki et al., 2023). The difference between ours and Oulhaj et al. (2024) is that, for extracting complex data structure, we employ a neural network, which holds the universal approximation theorem (Shalev-Shwartz and Ben-David, 2014).
2. We design a specialized mapper algorithm to visualize a summary of plausible paths with chemical structural changes using the generic one, based on theoretical guarantees. Then, we apply this specialized algorithm to the public 50S-ribosomal dataset used in Zhong et al. (2020). As a result, we confirm that a visualized graph summarizing the ribosomal conformational pathways by our method is consistent with an existing graph, which was manually constructed by Davis et al. (2016, Figure 7). Furthermore, our running time to compute the graph is much shorter than the counterpart of Yamazaki et al. (2023).

The present paper is organized as follows. In Section 2, we describe related work to our method. In Section 3, we give a detailed account of our method with theoretical guarantees. In Section 4, we show the results obtained in our numerical experiments using a ribosomal dataset. Finally, we conclude this study and discuss our future work in Section 5.

2. Related Work

In this section, we first review cryoTWIN (Yamazaki et al., 2023), and then describe details of existing mapper algorithms.

2.1. Revisit of cryoTWIN

Yamazaki et al. (2023) proposed a method to automatically compute a plausible protein conformational pathway from the single particle cryo-EM images. In their method, first, an auto-encoder named cryoTWIN is trained on the images, and the trained auto-encoder’s latent space is isometric to a space of 3D density maps. Then, a plausible protein conformational pathway as a sequence of 3D protein density maps is computed via the isometric latent space.

2.1.1. CryoTWIN

CryoTWIN is an auto-encoder consisting of an encoder Enc_ζ , a decoder g_ξ , and a latent distributional model P_ψ , where ζ, ξ, ψ are trainable parameters. Then the encoder outputs the latent variable z as input of a Fourier transformed cryo-EM image x . The latent model is defined as a Gaussian Mixture Model (GMM) $P_\psi, \psi = \{(\pi_k, \mu_k, \Sigma_k)\}_{k=1}^{\tilde{K}}$, where π_k, μ_k , and Σ_k represent k -th Gaussian’s weight, mean, and variance, respectively. Let x_i be a Fourier transformation of i -th cryo-EM image. The training objective is as follows:

$$\theta^*, \phi^*, \psi^* = \arg \min_{\theta, \phi, \psi} \frac{1}{N} \sum_{i=1}^N \mathbb{E}_\varepsilon \left[\underbrace{\|W \odot (x_i - \hat{x}_{z_i+\varepsilon})\|_2^2}_{\text{distortion}} + \beta \underbrace{(-\log P_\psi(z_i))}_{\text{rate}} \right],$$

where the symbols N, ε, \odot , and β are the number of cryo-EM images, random noise, Hadamard product, and the positive hyper-parameter, respectively. In addition, $\hat{x}_{z_i+\varepsilon} = g_\xi(z_i + \varepsilon, \hat{R}_i)$, $z_i = \text{Enc}_\zeta(x_i)$, \hat{R}_i is the corresponding estimated pose orientation to x_i , and $\hat{x}_{z_i+\varepsilon}$ is the predicted 2D Fourier image in the 3D Fourier volume. The symbol W is a weight matrix for introducing the isometricity; see Yamazaki et al. (2023, Appendix A). This objective is inspired by rate-distortion theory (Cover, 1999), like RaDOGAGA (Kato et al., 2020). After the training, for a latent variable z , the corresponding 3D density map \hat{V}_z is reconstructed by the trained decoder g_{ξ^*} .

2.1.2. Pathway Computing Algorithm

Since the latent space of the trained cryoTWIN is locally isometric to a space of 3D density maps, plausible conformational pathways can be computed via the trained GMM P_{ψ^*} using the decoder g_{ξ^*} ; see Algorithm 1 in Yamazaki et al. (2023). This algorithm requires two means μ_i^* and μ_j^* as start and end points of the pathway. Then, a Max-Flux path (Huo and Straub, 1997) on P_{ψ^*} between μ_i^* and μ_j^* is approximately computed using greedy optimization technique. The following minimization problem is used in the greedy optimization at $t + 1$ -th iteration to compute the $t + 1$ -th latent variable $z^{i \rightarrow j}(t + 1)$:

$$z^{i \rightarrow j}(t + 1) = \underset{\{z\}}{\operatorname{argmin}} \frac{1}{P_{\psi^*}(z)} \|z - z^{i \rightarrow j}(t)\|_2,$$

where $\{z\}$ is a set of the random latent variables. The path on P_{ψ^*} is expressed as a sequence of the latent variables: $(\mu_i^*, \dots, z^{i \rightarrow j}(t), \dots, \mu_j^*)$. Thereafter, by decoding each element in the sequence $(\mu_i^*, \dots, z^{i \rightarrow j}(t), \dots, \mu_j^*)$ using g_{ξ^*} , the algorithm outputs a sequence of 3D density maps $(\hat{V}_{\mu_i^*}, \dots, \hat{V}_{z^{i \rightarrow j}(t)}, \dots, \hat{V}_{\mu_j^*})$.

2.1.3. Preliminary Experiments

In the numerical experiments in Yamazaki et al. (2023), the authors showed several plausible conformational pathways of the 50S-ribosomal dataset, while focusing on significant μ_i^* . According to Yamazaki et al. (2023), the number of significant means μ^* are 30. Thus, the number of pairs (μ_i^*, μ_j^*) is around 450. In our preliminary experiments, we first employ the same hyper-parameters and computational resources with Yamazaki et al.

(2023, Section 4). Then, we compute all 450 conformational pathways to summarize the pathways. As a result, the running time based on the parallel computing is around 240 minutes.

2.2. Review of the Mapper Algorithm

In this section, we introduce the definition of the Mapper algorithm first. Thereafter, we introduce existing mapper techniques, in particular, which are applied to biological research domains.

2.2.1. Definition of Mapper Algorithm

Let X be a topological space and let $f: X \rightarrow \mathbb{R}$ be a continuous function called a *filter function*. We define an equivalence relation between two elements x and y in X by $x \sim_f y$ if and only if x and y are in the same connected component of $f^{-1}(z)$ for some z in $f(X)$. We then define the Reeb graph as follows.

Definition 1. (*Reeb Graph*) *The Reeb graph $\mathcal{R}_f(X)$ of a topological space X computed with a filter function f is the quotient space X/\sim_f .*

The Mapper, introduced in Singh et al. (2007), is a statistical version of the Reeb graph consisting of a computable approximation. It is discrete in the sense that it is computed on a finite metric space $(\mathbb{X}_n = \{x_0, \dots, x_n\} \subseteq X, d_X)$ with a continuous filter function f , where d_X is a metric on X . The procedure to compute a Mapper graph is as follows (Chazal and Michel, 2021):

1. Cover the range of values $f(\mathbb{X}_n)$ with a set of consecutive intervals $(I_s)_{1 \leq s \leq S}$ that overlap.
2. Apply a clustering algorithm to each pre-image $f^{-1}(I_s)$, $s \in \{1, \dots, S\}$. This produces a cover $\mathcal{C} = \{\mathcal{C}_{1,1}, \dots, \mathcal{C}_{1,K_1}, \dots, \mathcal{C}_{S,1}, \dots, \mathcal{C}_{S,K_S}\}$ of \mathbb{X}_n called the *pullback cover*, where $\mathcal{C}_{s,k}$ is the k -th cluster of $f^{-1}(I_s)$.
3. The Mapper graph is the 1-skeleton of the nerve complex of \mathcal{C} . It is a graph with a vertex $v_{s,k}$ for each $\mathcal{C}_{s,k}$, and an edge between two vertices $v_{s,k}$ and $v_{s',k'}$ if and only if $\mathcal{C}_{s,k} \cap \mathcal{C}_{s',k'} \neq \emptyset$.

See the complementary information in Appendix A.

2.2.2. Existing Mapper Algorithms

In this subsection, we introduce existing Mapper techniques focusing on biological research areas since the range of applications of Mapper techniques are fairly vast. In Wang et al. (2018), the Mapper algorithm is compared to other visualization methods, like t-SNE (van der Maaten and Hinton, 2008) and PCA, in the context of single-cell RNA sequencing data analysis. Notably, a filter function based on gene co-expression network analysis is used. Mapper graphs are shown to conserve the continuous nature in gene expression profiles, while also differentiating different cell types successfully. In Dehghanpoor et al. (2021), the Mapper algorithm is used to evaluate a preexisting protein conformational space exploration tool, that combines Rapidly-exploring Random Trees algorithm

and Monte Carlo criteria. Regular PCA directions are used as a multidimensional filter function. The resulting graph shows clusters that are identified as known conformations, while its topology is found to respect an energy criteria. Mapper graphs represent topological structure of high-dimensional data as graphs which can be regarded as a 1-dimensional simplicial complex. In Imoto and Hiraoka (2023), the authors adopted the Mapper algorithm to data with velocity, and associated flow on edges of the resulting Mapper graph. They applied their method to single-cell gene expression and combined their method with the Hodge decomposition on a graph to enhance the interpretation of the flow on the mapper graph.

The Mapper graph can also capture various features in data which has a complicated structure. It is also known that Mapper algorithm is less sensitive the distance metric than non-linear dimensional reduction or geometric embedding method. The authors of Yao et al. (2009) applied Mapper algorithm to characterize transient intermediate or transition state which are quite crucial for the description of biomolecular folding pathways. In Nicolau et al. (2011), a Disease-Specific Genomic Analysis is first performed on a breast cancer dataset to produce measures of deviation between tumor and normal tissue. This information is then introduced to the Mapper algorithm as a filter function. Due to its ability to conserve topological information in the dataset, the resulting graph reveals a region that corresponds to a unique mutational profile, that is otherwise scattered across different clusters in a regular clustering analysis.

A relaxed and more general version of the Mapper graph, that enjoys improved stratification properties, is introduced in Oulhaj et al. (2024). It is then used to optimize parameterized filter functions for regular Mapper graphs, with respect to a topological risk based on persistent homology. This is shown to produce quality Mapper graphs for 3-dimensional shapes and single cell RNA-sequencing data. The filter functions that are investigated in these experiments belong to a linear family and, as such, to the best of our knowledge, our work constitutes the first use of a deep neural network as a Mapper filter function.

3. Proposed Method

In this section, we introduce a generic entire procedure to compute an optimized Mapper graph which contains plausible conformational pathways. After formulating the method, we then introduce an *Energy-loss* based on existing reaction path optimization methods (see Huo and Straub (1997)), that serves as an optimization objective in our Mapper setting.

3.1. General Mapper Graph Optimization

Our approach focuses on the Mapper algorithm to produce pathways between conformations. We firstly show a generic algorithm for a computation of a Mapper graph in Algorithm 1. Algorithm 1 takes a set of latent variables as an input. Then we compute a loss from a Mapper graph which is constructed with a parameterized filter function. For the construction of the Mapper graph, note that one can apply arbitrary clustering

Algorithm 1: Generic computation of a Mapper graph

Input:

- $\{z_i\}_{i=1}^N$: a set of latent variables,
- P_ψ : a trained GMM with $\psi = \{(\pi_k, \mu_k, \Sigma_k)\}_{k=1}^{\tilde{K}}$,
- \tilde{K} : the number of influential mean vectors in P_ψ ,
- $\bar{K} (< \tilde{K})$: a natural number,
- κ : the number of neighbors,
- $r \in (0, 1)$: an overlap rate,
- K : the maximum number of clusters,
- f_θ : a filter function parameterized by trainable parameters θ ,
- λ : a positive value.

Output: An optimized mapper graph.

- 1 Using κ , build a kNN graph $G = (\mathcal{V}, \mathcal{E})$ on $\{z_i\}_{i=1}^N$, where $\mathcal{V} = \{z_i\}_{i=1}^N$ and \mathcal{E} is the set of the edges.
 - 2 Find top \bar{K} largest values in $P_\psi(\mu_k), k = 1, \dots, \tilde{K}$, and define the corresponding Gaussian indexes as $k_j (j = 1, \dots, \bar{K})$, where $P_\psi(\mu_{k_j}) \leq P_\psi(\mu_{k_{j+1}})$.
 - 3 **for** each epoch **do**
 - 4 Construct a Mapper graph on $\{z_i\}_{i=1}^N$ based on f_θ and a specific cluster algorithm.
 - 5 Compute a loss L_θ based on the resulting Mapper graph M_θ
 - 6 Compute a regularization term $\text{Reg}(G) := \lambda \sum_{(i,j) \in \mathcal{E}} (f_\theta(z_i) - f_\theta(z_j))^2$ based on G .
 - 7 $L_\theta \leftarrow L_\theta + \text{Reg}(G)$.
 - 8 Minimize L_θ with respect to the parameters θ .
 - 9 **return** the final Mapper graph.
-

algorithm. As a technique to incorporate topological information into the loss, we build a kNN graph on top of the input dataset, and add a regularization term to the loss. Finally, we update the parameters so as the value of the loss decrease. In this way, we obtain an optimized Mapper graph as the output.

3.2. Specialized Mapper Graph Optimization

The Mapper algorithm is applied to a large sample of latent space variables with a fixed number of intervals and a fixed overlap. Two main features are introduced in our Mapper based method:

1. The clustering method is based on the GMM distribution that is assumed to be that of the latent variables and estimated beforehand. The exact method is described in Algorithm 3. This approach guarantees that the nodes in the Mapper correspond to clusters that regroup conformations which are structurally similar.
2. The filter function is given by a neural network that acts on a feature transform of

the latent space. Specifically, the filter function has the form of

$$f_{\theta}(z) = DNN_{\theta}(T(z)),$$

where DNN_{θ} is a deep neural network. Let $\{\mu_i, \Sigma_i\}_{i \in I}$ denote Gaussian distribution parameters corresponding to notable conformations in the latent space. We also define a transformation T of a latent variable z with respect to μ_i and Σ_i as follows:

$$T: z \mapsto \left((z - \mu_i)^{\top} \cdot \Sigma_i \cdot (z - \mu_i) \right)_{i \in I}.$$

The neural network is introduced for its ability to approximate a large class of functions, allowing for a filter function that stratifies the latent space in a way that detects conformational pathways. The parameters θ are then optimized to minimize the total Energy-loss inside the pathways described by the Mapper graph. More details about the specific loss used are given in Algorithm 5. The parameters $\{\mu_i, \Sigma_i\}_{i \in I}$ can be taken from the Gaussian mixture model that is fit on the latent variables during the training of the auto-encoder. Components that correspond to conformations of interest can be selected with respect to their scale in the GMM distribution. By means of the order with which the filter function stratifies the latent space, the resulting Mapper graph topology and the cluster representatives are all controlled by the deep neural network. Depending on the complexity of the chosen neural network architecture, conformational paths of interest are produced by our method. More details on this are given in Section 4. In order to approach the continuous Energy-loss associated to the paths described by a Mapper graph built on the latent space dataset, we compute a modified discrete Energy-loss where distances are given locally by variations in the filter values, by taking into account the gradient of the filter and using a first order Taylor approximation; see Algorithm 4. The total loss associated to a set of parameters θ is

$$L_{\theta} = \text{Energy-loss}(M_{\theta}, f_{\theta}, n_{\text{steps}}).$$

This total loss serves as an optimization objective in our setting; see Algorithm 5.

We now give a specialized method to optimize a Mapper graph which contains meaningful conformational pathways in Algorithm 2. All the algorithms used in Algorithm 2 can be found in Algorithms 3, 4, and 5. The step count n_{steps} in Algorithm 5 is chosen to be fairly large without impacting running time, in accordance with the theoretical guarantees relating to convergence given in Section 3.3. It should also be noted that choosing n_{steps} to be too large can result in poor results, as the pathways that are used to compute the loss become too long. The loss L_{θ} is minimized using the *Adam* variant of stochastic gradient descent (Kingma and Ba, 2015).

3.3. Theoretical Guarantees for Energy-Loss

We mathematically prove that computing plausible pathways in the latent space is equivalent to that in the output space of cryoTWIN. Hence, the theoretical guarantees presented in this section justify the use of random samples to detect pathways on one

Algorithm 2: Specialized computation of a conformational Mapper graph

Input:

- $\{z_i\}_{i=1}^N$: set of latent variables,
- P_ψ : trained GMM with $\psi = \{(\pi_k, \mu_k, \Sigma_k)\}_{k=1}^{\bar{K}}$,
- κ : number of neighbors,
- $\bar{K} (< \tilde{K}), S, B$: natural numbers,
- $r \in (0, 1)$: overlap rate,
- K : maximum number of clusters,
- f_θ : filter function defined by a deep neural network parameterized by trainable parameters θ ,
- λ : positive value.

Output: An optimized conformational mapper graph.

- 1 Using κ , build a kNN graph $G = (\mathcal{V}, \mathcal{E})$ on $\{z_i\}_{i=1}^N$, where $\mathcal{V} = \{z_i\}_{i=1}^N$ and \mathcal{E} is the set of the edges.
 - 2 Find top \bar{K} largest values with $P_\psi(\mu_k), k = 1, \dots, \bar{K}$, and define the corresponding Gaussian indexes as $k_j (j = 1, \dots, \bar{K})$, where $P_\psi(\mu_{k_j}) \leq P_\psi(\mu_{k_{j+1}})$.
 - 3 **for** each epoch **do**
 - 4 Using $\{z_i\}_{i=1}^N$, a filter function $f_\theta, S \in \mathbb{N}$, and $r \in (0, 1)$, compute a set of the intervals $\{I_s\}_{s=1}^S$; see Section 2.2.1.
 - 5 Then, conduct the GMM clustering (see Algorithm 3) for each interval.
 - 6 Based on the above clustering result, construct the mapper graph $M_\theta = (\tilde{\mathcal{V}}_\theta, \tilde{\mathcal{E}}_\theta)$; see Section 2.2.1.
 - 7 Set the energy-loss L_θ to zero, and update M_θ via minimization of L_θ w.r.t. θ , as follows:
 - 8 **for** each $(\mathcal{C}, \mathcal{C}') \in \tilde{\mathcal{E}}_\theta$ **do**
 - 9 First, sort the latent variables in $\mathcal{C} \cup \mathcal{C}'$ based on the filter value in ascending order.
 - 10 Secondly, let $\iota(b)$ denote the $\lfloor \frac{b(|\mathcal{C} \cup \mathcal{C}'| - 1)}{B} \rfloor$ -th index of the corresponding latent variable in the order, where $b \in \{1, \dots, B\}$.
 - 11 Thirdly, $L_\theta + = \sum_{b=1}^{B-1} \frac{1}{P_\psi\left(\frac{z_{\iota(b)} + z_{\iota(b+1)}}{2}\right)} \text{LDA}(z_{\iota(b)}, z_{\iota(b+1)}, f_\theta, \nabla f_\theta(z_{\iota(b)}))$; see the function LDA in Algorithm 4.
 - 12 Compute a regularization term $\text{Reg}(G) := \lambda \sum_{(i,j) \in \mathcal{E}} (f_\theta(z_i) - f_\theta(z_j))^2$ based on G .
 - 13 $L_\theta \leftarrow L_\theta + \text{Reg}(G)$.
 - 14 $\theta \leftarrow \arg \min_\theta L_\theta$.
 - 15 **return** the final mapper graph M_θ .
-

hand, and gives insurance to using the latent space to achieve this task on the other. We note that the similar statement can be found in Yamazaki et al. (2023) without a proof.

Consider the case where we are interested in an optimal conformational path between

Algorithm 3: GMM based clustering for each interval

Input:

$\{z_i\}_{i=1}^N$: dataset of latent variables,
 $\{(\pi_k, \mu_k, \Sigma_k)\}_{k=1}^{\bar{K}}$: GMM parameters of interest,
 K : maximum number of clusters.

Output: An estimated label of each sample z_i .

- 1 **for** $1 \leq k \leq \bar{K}$ **do**
 - 2 $L_k \leftarrow \max_{i \in \{1, \dots, N\}} \pi_k \cdot P_k(z_i)$, where P_k is the k -th highest Gaussian probability density with parameters.
 - 3 Candidates \leftarrow indices of the K -biggest values in $\{L_k\}_{k=1}^{\bar{K}}$
 - 4 **for** $1 \leq i \leq N$ **do**
 - 5 Label $_i \leftarrow \arg \max_{k \in \text{candidates}} \pi_k \cdot P_k(z_i)$
 - 6 **return** $\{\text{Label}_i\}_{i=1}^N$.
-

Algorithm 4: Local Distance Approximation (LDA)

Input:

$z, z' \in \mathbb{R}^d$: points,
 f : a filter function,
 $\nabla f(z)$: the gradient of f at z .

- 1 **for** $i \in \{1, \dots, d\}$ **do**
 - 2 $\tilde{z}_i \leftarrow (z_1, \dots, z'_i, \dots, z_d)$, $\partial f_i \leftarrow f(z) - f(\tilde{z}_i)$.
 - 3 **return** $\left\| \left(\frac{\partial f_i}{\nabla f(z)_i} \right)_{i \in \{1, \dots, d\}} \right\|_2$.
-

Algorithm 5: Energy-loss

Input:

(V, E) : a Mapper graph,
 f : a filter function,
 n_{steps} : the number of steps.

- 1 **for** $(c_i, c_j) \in E$ **do**
 - 2 Order $c_i \cup c_j$ by filter value as $\{z_k\}_{k=0}^{|c_i \cup c_j| - 1}$ where for any $k \in \{0, \dots, |c_i \cup c_j| - 2\}$, $f(z_k) \leq f(z_{k+1})$.
 - 3 index(k) $\leftarrow \lfloor \frac{k \cdot (|c_i \cup c_j| - 1)}{K} \rfloor$, for any $k \in \{1, \dots, n_{\text{steps}}\}$.
 - 4 $l_{(c_i, c_j)} := \sum_{k=1}^{n_{\text{steps}} - 1} \frac{1}{P\left(\frac{z_{\text{index}(k)} + z_{\text{index}(k+1)}}{2}\right)} \text{LDA}(z_{\text{index}(k)}, z_{\text{index}(k+1)}, f, \nabla f(z_{\text{index}(k)}))$.
 - 5 **return** $\sum_{(c_i, c_j) \in E} l_{(c_i, c_j)}$.
-

two protein conformation representations z_0 and z_∞ , where $z_0, z_\infty \in \mathbb{R}^d$ ($d \in \mathbb{N}$). We also

assume that we know a closed form $P: \mathbb{R}^d \rightarrow [0, +\infty)$ for the probability density of the protein conformation representations, and $P(\mathbb{R}^d)$ is connected.

We denote by $\text{PC}^0([0, 1], \mathbb{R}^d)$ the set of piecewise continuous functions $f: [0, 1] \rightarrow \mathbb{R}^d$, that satisfy $f(0) = z_0$ and $f(1) = z_\infty$. A function $f \in \text{PC}^0([0, 1], \mathbb{R}^d)$ will be called a *conformational path* between z_0 and z_∞ . For $f \in \text{PC}^0([0, 1], \mathbb{R}^d)$, we define its Energy-loss I_f as follows.

Definition 2. (*Energy-loss*) Let $f \in \text{PC}^0([0, 1], \mathbb{R}^d)$. The Energy-loss associated to f is

$$I_f := \int_0^1 \frac{1}{P(f(t))} df(t).$$

The integral above, called a line integral, is defined as the following Riemann integral

$$\int_0^1 \frac{1}{P(f(t))} df(t) := \lim_{n \rightarrow \infty} \sum_{i=0}^{n-1} \frac{1}{P\left(\frac{f\left(\frac{i}{n}\right) + f\left(\frac{i+1}{n}\right)}{2}\right)} \left\| f\left(\frac{i+1}{n}\right) - f\left(\frac{i}{n}\right) \right\|_2.$$

The optimal Energy-loss for all possible conformational paths is defined as

$$S^* := \inf_{f \in \text{PC}^0([0, 1], \mathbb{R}^d)} I_f.$$

3.3.1. Convergence of Energy-Loss

In our work, we wish to approach the optimal Energy-loss by using a finite N sample $\{z_j\}_{j=1}^N$ of conformations, that independently follow a distribution of density P . We then discretize the Energy-loss using n_{steps} steps. Precisely, we define the following stochastic loss as follows.

Definition 3. (*Stochastic Energy-loss*) Let $\{z_j\}_{j=1}^N \subseteq \mathbb{R}^d$ be a random sample drawn independently from a distribution of density P and $n_{\text{steps}} \in \mathbb{N}$ such that $n_{\text{steps}} > 2$. The stochastic Energy-loss with n_{steps} steps associated to $\{z_j\}_{j=1}^N$ is

$$S_{n_{\text{steps}}}^{(N)} := \min_{\{z_i\}_{i=1}^{n_{\text{steps}}-1} \subseteq \{z_j\}_{j=1}^N} \sum_{i=0}^{n_{\text{steps}}-1} \frac{1}{P\left(\frac{z_i + z_{i+1}}{2}\right)} \|z_{i+1} - z_i\|_2,$$

with the convention $z_K = z_\infty$.

The theoretical part of our work aims at proving that $S_{n_{\text{steps}}}^{(N)}$ gets arbitrarily close to S^* when N and n_{steps} go to infinity. In order to properly define this property in terms of real sequence convergence and random variable sequence convergence, we introduce the following quantity:

Definition 4. (*Discrete Optimal Energy-loss*) Let $n_{\text{steps}} \in \mathbb{N}$ such that $n_{\text{steps}} > 2$. The discrete optimal Energy-loss with n_{steps} steps is

$$S_{n_{\text{steps}}} := \inf_{\{z_i\}_{i=1}^{n_{\text{steps}}-1} \subseteq \mathbb{R}^d} \sum_{i=0}^{n_{\text{steps}}-1} \frac{1}{P\left(\frac{z_i + z_{i+1}}{2}\right)} \|z_{i+1} - z_i\|_2,$$

with the same convention $z_{n_{\text{steps}}} = z_\infty$.

We have the following result regarding the different losses that we defined above.

Theorem 1.

$$S_{n_{\text{steps}}} \xrightarrow[n_{\text{steps}} \rightarrow \infty]{} S^*. \quad (1)$$

Moreover, for every $n_{\text{steps}} \in \mathbb{N}$ such that $n_{\text{steps}} > 2$, assuming that

1. The density P is continuously differentiable.
2. The density P is strictly positive almost everywhere.
3. We now only consider discrete paths $\{z_i\}_{i=1}^{n_{\text{steps}}-1} \subseteq \mathbb{R}^d$ such that $\forall i \in \{0, \dots, n_{\text{steps}}-1\}$
 $z_{i+1} \neq z_i$

Then we have

$$S_{n_{\text{steps}}}^{(N)} \xrightarrow[N \rightarrow \infty]{a.s.} S_{n_{\text{steps}}}. \quad (2)$$

3.3.2. Relating Electronic Density Space to Latent Space with Energy-Loss

We consider the case where protein conformations can be determined by three dimensional electronic density maps as well as by lower dimensional latent representations. Typically, in the first case, the representations consist of electronic density values on a three dimensional cubic grid of resolution γ , while the latent representations are real vectors of dimension p .

We suppose that we have access to a decoder function $g_\xi: \mathbb{R}^d \rightarrow \mathbb{R}^{\gamma^3}$ that decodes the latent representations into the corresponding electronic densities. We also suppose that all the electronic densities of interest are in the image of the decoder $g_\xi(\mathbb{R}^d)$. In practice, this setting can arise from a Cryo-EM imagery decoding machine learning model. Given a probability density $P_{\text{ed}}: g_\xi(\mathbb{R}^d) \rightarrow [0, +\infty)$ on the space of electronic densities, we turn our interest to the optimal Energy-loss on this space, and to how it translates to the latent space given the decoder g_ξ . We denote

$$S_{\mathbb{R}^d}^* := \inf_{f \in \text{PC}^0([0,1], \mathbb{R}^d)} \int_0^1 \frac{1}{P(f(t))} df(t),$$

and

$$S_{g_\xi(\mathbb{R}^d)}^* := \inf_{g \in \text{PC}^0([0,1], g_\xi(\mathbb{R}^d))} \int_0^1 \frac{1}{P_{\text{ed}}(g(t))} dg(t).$$

We call $S_{\mathbb{R}^d}^*$ and $S_{g_\xi(\mathbb{R}^d)}^*$ respectively the *optimal Energy objectives* in the latent space and the electronic density space respectively.

Lemma 1. (*Probability measure of electronic densities*) Let V be a random variable valued in $g_\xi(\mathbb{R}^d)$. Assume that it admits a probability density $P_{\text{ed}} := g_\xi(\mathbb{R}^d) \rightarrow [0, +\infty)$ with respect to the measure $\mu \circ g_\xi^{-1}$, with μ being the Lebesgue measure in \mathbb{R}^d . We denote by $P := \mathbb{R}^d \rightarrow [0, +\infty)$ the probability density of $z = g_\xi^{-1}(V)$ with respect to μ . Then we have $P_{\text{ed}} = P \circ g_\xi^{-1}$.

Lemma 2. (*Stability of the optimal Energy-loss by composition with the decoder*) Assume that the decoder g_ξ is a topological embedding, i.e., that it is a homeomorphism from \mathbb{R}^d to $g_\xi(\mathbb{R}^d)$. Then we have

$$\inf_{g \in \text{PC}^0([0,1], g_\xi(\mathbb{R}^d))} \int_0^1 \frac{1}{P_{ed}(g(t))} dg(t) = \inf_{f \in \text{PC}^0([0,1], \mathbb{R}^d)} \int_0^1 \frac{1}{P_{ed}(g_\xi \circ f(t))} dg_\xi \circ f(t).$$

Theorem 2. (*Correspondence between Energy objectives in the latent space and the electronic density space*) Let z be a random variable valued in \mathbb{R}^d , having probability density P . Assume that

1. P_{ed} is the probability density of $V = g_\xi(z)$ with respect to the measure $\mu \circ g_\xi^{-1}$,
2. the decoder g_ξ is a topological embedding,
3. the decoder g_ξ verifies the following local approximate isometry property

$$\exists C > 0, \exists \epsilon > 0, \forall z, z' \in \mathbb{R}^d, \|z - z'\|_2 \leq \epsilon \Rightarrow \|g_\xi(z) - g_\xi(z')\|_2 = C \cdot \|z - z'\|_2.$$

Then we have that for any $f \in \text{PC}^0([0, 1], \mathbb{R}^d)$,

$$\int_0^1 \frac{1}{P_{ed}(g_\xi \circ f(t))} dg_\xi \circ f(t) = C \cdot \int_0^1 \frac{1}{P(f(t))} df(t). \quad (3)$$

We also have

$$S_{g_\xi(\mathbb{R}^d)}^* = C \cdot S_{\mathbb{R}^d}^*. \quad (4)$$

We remark that the assumptions in Theorems 1 and 2 are verified by cryoTWIN and were written specifically with its setting in mind. However, these theorems are given here for arbitrary auto-encoders that verify the stated assumptions.

4. Numerical Experiments

4.1. Setting

We use our method on the L17-depleted 50S Ribosomal intermediates dataset (EMPIAR-10076) Davis et al. (2016). A CryoTWIN model is fit on this dataset beforehand, which gives us access to the GMM parameters of the latent space distribution. As described, certain Gaussian components are used to extract learning features from the dataset and to perform clustering. Here, they correspond to 11 components, chosen to be all different by visual inspection of their decoded densities and belonging to the 20 most influential components with respect to their scale in the GMM distribution.

4.2. Parameter Selection

We first fix the following parameters used to create the Mapper graph:

- **Number of intervals S :** 25,
- **Overlap rate r :** 0.25,
- **Maximum number of clusters in each interval K :** 5,
- **Number of steps N_{steps} :** 10^2 ,
- **Number of mean vectors \bar{K} :** 24,
- **Number of neighbors of the kNN graph κ :** 15.

We then run 300 optimization iterations for different filter neural network architectures with learning rate value 10^{-3} . The neural networks used consist of successive dense layers with rectifier activation functions (ReLU). We refer to each architecture by the total number of layers n_{layers} and the number of units n_{units} in each intermediate layer.

We use a filter function that consists of a single layer. This corresponds to the following filter function form:

$$f_{\theta}: z \mapsto \langle T(z), \theta \rangle,$$

with $\theta \in \mathbb{R}^{11}$. We optimize the loss L_{θ} with respect to the parameters θ for 300 iterations.

4.3. Result and Discussion

Regarding the number of layers of the filter function, we run experiments under several conditions. Through them, we empirically confirmed that the most simple neural network architecture achieves the best optimization result. We justify this by pointing at the feature transformation T that is introduced before the neural network. It gives information about the main conformations that are present in the dataset while the neural network part of the filter needs to map them to \mathbb{R} in an order that respects the chemical transformations possible between them. This can be achieved by one layer, as the coefficient given to each feature can be tuned to place its corresponding conformation arbitrarily in \mathbb{R} .

Experiments show that the optimization result is highly dependent on the initial state. This is due to the roughness of the objective, which is only smooth in subsets of the parameter space.

We evaluate the pathways given in the Mapper graph using the manually constructed conformational graph given in Davis et al. (2016, Figure 7).

The nodes in the resulting mapper graph can be labeled in the same way their corresponding clusters were constructed in Algorithm 3. A node is given the conformation label of the GMM component with the highest probability of a point in the cluster belonging to it. The GMM components are labeled beforehand using visual inspection. The labeled Mapper graph is in Figure 1. We constructed the labeled Mapper graph presented in Figure 1 in range of 40–45 minutes using Apple M1 (16 GB, 8 cores).

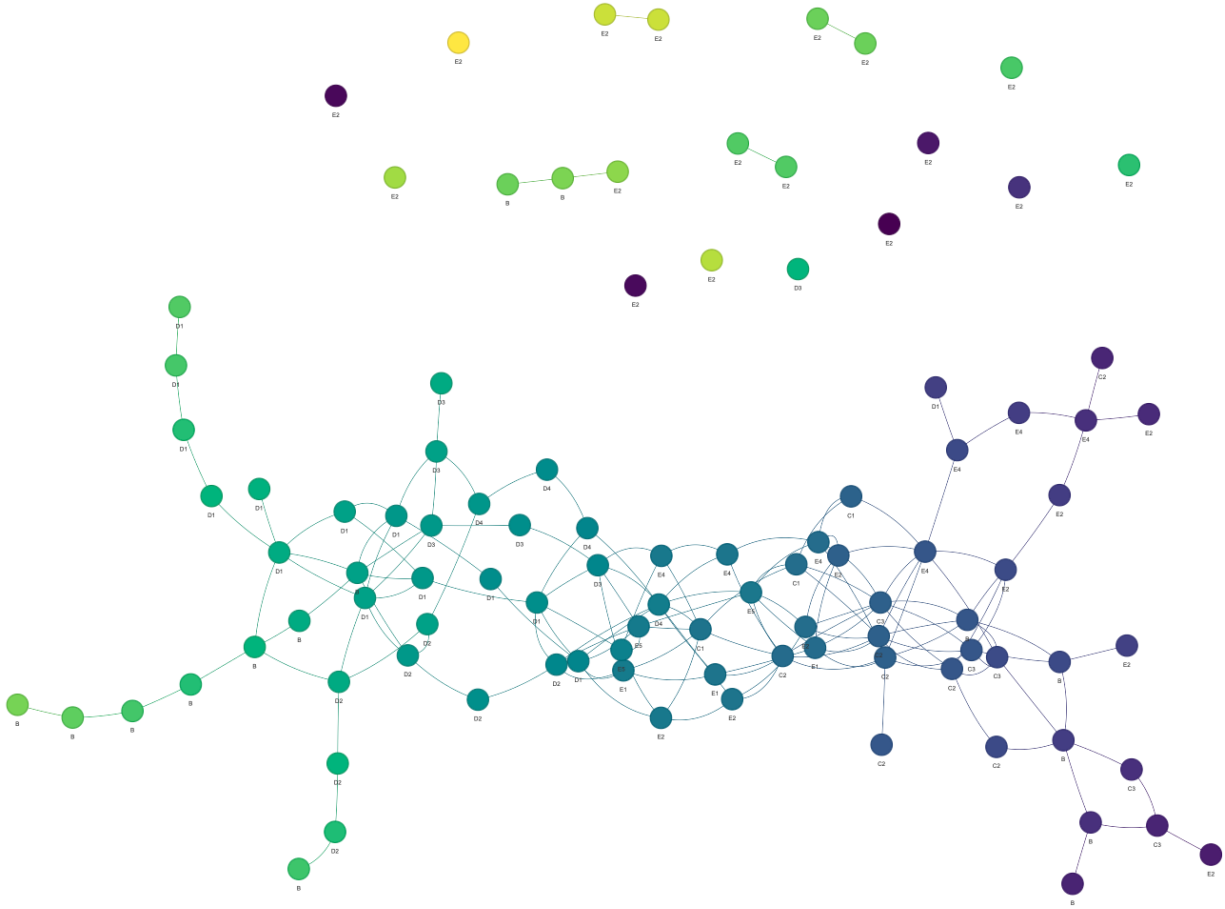


Figure 1: Labeled optimized Mapper graph. The label of each cluster is that of its representative GMM mean.

Several points below can be drawn from the comparison of Davis' graph and Figure 1. We note that E3 is absent from the graph because it did not correspond to one of the 30 GMM components used.

- The Mapper graph captured three accurate pathways ($B \rightarrow D1 \rightarrow E1 \rightarrow E2 \rightarrow E4 \rightarrow E5$, $B \rightarrow C2 \rightarrow E1 \rightarrow E2 \rightarrow E4 \rightarrow E5$, and $B \rightarrow C2 \rightarrow C3 \rightarrow C1 \rightarrow E4 \rightarrow E5$), which are given in the Davis' graph. For the rest pathway ($B \rightarrow D1 \rightarrow D2 \rightarrow D4 \rightarrow E5$), it is almost exact except the lack of label D3.
- The Mapper graph captured the differentiation of label B into labels C and D.
- The Mapper graph captured the entire distribution of labels B, C, D, and E.
- The Mapper graph separated clusters of labels C and D, which should not be connected each other.

5. Conclusion and Future Work

We introduced a method based on the Mapper algorithm for visualizing protein conformational pathways in unsupervised manner. We based this method on preexisting auto-encoder models that reconstruct protein 3-dimensional electronic densities from cryo-EM images. Our method uses a parameterized filter function by deep neural network in order to automatically detect pathways of interest inside the latent space of trained auto-encoders, on top of using Gaussian mixture model based clustering. We experimented on a ribosomal intermediates dataset and found that our constructed Mapper graph captures several features when compared to a manually created pathway graph based on biological knowledge. While our method fails to accurately reconstruct the connection of conformational pathways in some regions of the latent space, its unsupervised nature and its computational efficiency make it a fairly useful tool.

References

- Chapelle, O., Schlkopf, B., Zien, A., 2010. *Semi-Supervised Learning*. 1st ed., The MIT Press.
- Chazal, F., Michel, B., 2021. An introduction to topological data analysis: Fundamental and practical aspects for data scientists. *Frontiers in artificial intelligence* 4. doi:10.3389/frai.2021.667963.
- Cover, T.M., 1999. *Elements of information theory*. John Wiley & Sons.
- Davis, J.H., Tan, Y.Z., Carragher, B., Potter, C.S., Lyumkis, D., Williamson, J.R., 2016. Modular assembly of the bacterial large ribosomal subunit. *Cell* 167, 1610–1622.
- Dehghanpoor, R., Afrasiabi, F., Haspel, N., 2021. Using topological data analysis and rrt to investigate protein conformational spaces. *bioRxiv*, 2021–08.
- Earl, L.A., Falconieri, V., Milne, J.L., Subramaniam, S., 2017. Cryo-EM: beyond the microscope. *Curr. Opin. Struct. Biol.* 46, 71–78.
- Huo, S., Straub, J.E., 1997. The MaxFlux algorithm for calculating variationally optimized reaction paths for conformational transitions in many body systems at finite temperature. *Journal of Chemical Physics* 107, 5000–5006.
- Imoto, Y., Hiraoka, Y., 2023. V-mapper: topological data analysis for high-dimensional data with velocity. *Nonlinear Theory and Its Applications, IEICE* 14, 92–105.
- Kato, K., Zhou, J., Sasaki, T., Nakagawa, A., 2020. Rate-distortion optimization guided autoencoder for isometric embedding in euclidean latent space, in: *Proceedings of the 37th International Conference on Machine Learning, ICML 2020*, pp. 5166–5176.
- Kingma, D.P., Ba, J., 2015. Adam: A method for stochastic optimization, in: *International Conference on Learning Representations, ICLR 2015*.

- Kinman, L., Powell, B., Zhong, E., Berger, B., Davis, J., 2023. Uncovering structural ensembles from single-particle cryo-em data using cryodrgn. *Nature Protocols* 18, 319–339.
- van der Maaten, L., Hinton, G., 2008. Visualizing data using t-SNE. *Journal of Machine Learning Research* 9, 2579–2605.
- Nicolau, M., Levine, A.J., Carlsson, G., 2011. Topology based data analysis identifies a subgroup of breast cancers with a unique mutational profile and excellent survival. *Proceedings of the National Academy of Sciences* 108, 7265–7270.
- Oulhaj, Z., Carrière, M., Michel, B., 2024. Differentiable mapper for topological optimization of data representation. [arXiv:2402.12854](https://arxiv.org/abs/2402.12854).
- Shalev-Shwartz, S., Ben-David, S., 2014. *Understanding Machine Learning: From Theory to Algorithms*. Cambridge University Press, USA.
- Barroso da Silva, F.L., Carloni, P., Cheung, D., Cottone, G., Donnini, S., Foegeding, E.A., Gulzar, M., Jacquier, J.C., Lobaskin, V., MacKernan, D., Mohammad Hosseini Naveh, Z., Radhakrishnan, R., Santiso, E.E., 2020. Understanding and controlling food protein structure and function in foods: Perspectives from experiments and computer simulations. *Annual Review of Food Science and Technology* 11, 365–387.
- Singh, G., Mémoli, F., Carlsson, G.E., et al., 2007. Topological methods for the analysis of high dimensional data sets and 3d object recognition. *PBG@ Eurographics* 2, 091–100.
- Wang, T., Johnson, T., Zhang, J., Huang, K., 2018. Topological methods for visualization and analysis of high dimensional single-cell rna sequencing data, in: *BIOCOMPUTING 2019: Proceedings of the Pacific Symposium*, World Scientific. pp. 350–361.
- Wu, Z., Chen, E., Zhang, S., Ma, Y., Mao, Y., 2022. Visualizing conformational space of functional biomolecular complexes by deep manifold learning. *International Journal of Molecular Sciences* 23, 8872.
- Yamazaki, K., Wada, Y., Tokuhisa, A., Wada, M., Katoh, T., Umeda, Y., Okuno, Y., Nakagawa, A., 2023. An auto-encoder to reconstruct structure with cryo-em images via theoretically guaranteed isometric latent space, and its application for automatically computing the conformational pathway, in: *Medical Image Computing and Computer Assisted Interventions, MICCAI 2023*.
- Yao, Y., Sun, J., Huang, X., Bowman, G.R., Singh, G., Lesnick, M., Guibas, L.J., Pande, V.S., Carlsson, G., 2009. Topological methods for exploring low-density states in biomolecular folding pathways. *The Journal of chemical physics* 130.
- Zhong, E.D., Bepler, T., Berger, B., Davis, J.H., 2021. CryoDRGN: reconstruction of heterogeneous cryo-EM structures using neural networks. *Nature Methods* 18, 176–185.

Zhong, E.D., Bepler, T., Davis, J.H., Berger, B., 2020. Reconstructing continuous distributions of 3D protein structure from cryo-EM images, in: International Conference on Learning Representations, ICLR 2020.

Appendix A. Complements of the construction of a Mapper graph

There are a number of choices to be made when computing a Mapper from a point cloud : (i) **Choice of $(I_s)_{1 \leq s \leq S}$** : a popular practice when choosing a cover for the range of values of the filter is to choose intervals of the same length ℓ , where no more than two intervals can intersect at once. The overlap rate r between intervals is also constant (and is therefore less than $1/2$). By doing this, we can tune the cover through r and g . (ii) **Choice of the clustering algorithm** : It is possible to cluster the pre-images using any existing algorithm. Another popular choice however is to construct a δ -neighborhood graph and to look at its connected components as clusters. A δ -neighborhood graph is a graph with vertices corresponding to each point in \mathbb{X}_n and with an edge between two vertices if and only if the distance between the two points is less than δ .

A mesh of a human model in 3 dimensions is in Figure A.2. We wish to compute the mapper on the set of vertices of the mesh with the height coordinate as our filter function. We choose to cover the range of height values in the manner we described above, with 25 intervals of the same length with an overlap of 30%. For clustering, we use the KMeans algorithm with 3 clusters. The resulting graph is also represented in Figure A.2.

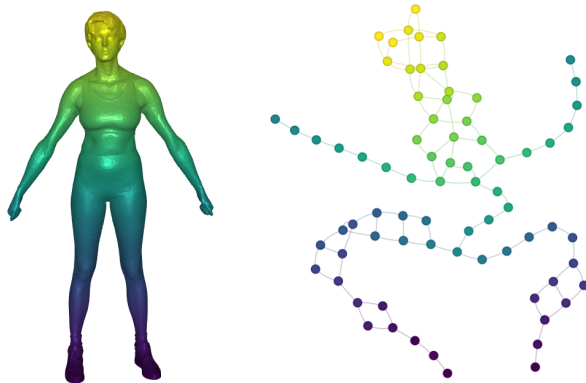


Figure A.2: On the left: 3-dimensional mesh of a human shape colored in terms of height. On the right: Mapper graph computed using the vertices of the mesh, height as a filter, 25 equal intervals with 30% overlap and KMeans clustering with 3 clusters.

Here, we represent the mean value of the filter function on each cluster using the color of its vertex in the Mapper graph. The Mapper graph we computed can be seen as a skeleton of the shape of a human : we can distinguish two legs, a torso and two arms.

Appendix B. Proofs

Appendix B.1. Proof of Equation (1)

Proof. We firstly show that $\{S_{n_{\text{steps}}}\}_{n_{\text{steps}} \geq 2}$ is lower bounded by 0 and non-increasing. Let $\{z_i\}_{i=1}^{n_{\text{steps}}-1} \subseteq \mathbb{R}^d$, and consider $\{z'_i\}_{i=1}^{n_{\text{steps}}} \subseteq \mathbb{R}^d$ such that $z'_1 = z_1$ and for any $i \in$

$\{2, \dots, n_{\text{steps}}\}$, $z'_i = z_{i-1}$ holds. Note that we always have $z_{n_{\text{steps}}} = z'_{n_{\text{steps}}+1} = z_\infty$. We then have

$$\sum_{i=0}^{n_{\text{steps}}-1} \frac{1}{P\left(\frac{z_i+z_{i+1}}{2}\right)} \|z_{i+1} - z_i\|_2 = \sum_{i=0}^{n_{\text{steps}}} \frac{1}{P\left(\frac{z'_i+z'_{i+1}}{2}\right)} \|z'_{i+1} - z'_i\|_2.$$

Accordingly, we have

$$\begin{aligned} & \left\{ \sum_{i=0}^{n_{\text{steps}}-1} \frac{1}{P\left(\frac{z_i+z_{i+1}}{2}\right)} \|z_{i+1} - z_i\|_2, \{z_i\}_{i=1}^{n_{\text{steps}}-1} \subseteq \mathbb{R}^d \right\} \\ & \subseteq \left\{ \sum_{i=0}^{n_{\text{steps}}} \frac{1}{P\left(\frac{z_i+z_{i+1}}{2}\right)} \|z_{i+1} - z_i\|_2, \{z_i\}_{i=1}^{n_{\text{steps}}} \subseteq \mathbb{R}^d \right\}. \end{aligned}$$

Therefore $S_{n_{\text{steps}}+1} \leq S_{n_{\text{steps}}}$ holds by the definition of the infimum. We showed that $\{S_{n_{\text{steps}}}\}_{n_{\text{steps}} \geq 2}$ is convergent, and we furthermore have

$$\lim_{K \rightarrow \infty} S_K = \inf_{K \geq 2} \{S_K\}.$$

We now show that this limit is exactly S^* . We firstly have $S^* \leq \lim_{K \rightarrow \infty} S_{n_{\text{steps}}}$ because for any $n_{\text{steps}} \geq 2$, $S^* \leq S_{n_{\text{steps}}}$ holds. Let $n_{\text{steps}} \in \mathbb{N}$ such that $n_{\text{steps}} > 2$, and fix a discrete path $\{z_i\}_{i=1}^{n_{\text{steps}}-1} \subseteq \mathbb{R}^d$. Then let us consider the piecewise constant function $g: [0, 1] \rightarrow \mathbb{R}^d$ such that for each $i \in \{0, \dots, n_{\text{steps}} - 1\}$ and for any $t \in [\frac{i}{n_{\text{steps}}}, \frac{i+1}{n_{\text{steps}}})$, $g(t) = z_i$ and $g(1) = z_\infty$ hold. We then have

$$I_g = \sum_{i=0}^{n_{\text{steps}}-1} \frac{1}{P\left(\frac{z_i+z_{i+1}}{2}\right)} \|z_{i+1} - z_i\|_2.$$

This is because the sequence of Riemann sums, which limit is by definition equal to I_g , is stationary after rank n_{steps} and its terms are equal to the sum above. Since $g \in \text{PC}^0([0, 1], \mathbb{R}^d)$,

$$S^* \leq \sum_{i=0}^{n_{\text{steps}}-1} \frac{1}{P\left(\frac{z_i+z_{i+1}}{2}\right)} \|z_{i+1} - z_i\|_2$$

holds for all $\{z_i\}_{i=1}^{n_{\text{steps}}-1} \subseteq \mathbb{R}^d$. Hence we conclude that $S^* \leq S_{n_{\text{steps}}}$.

We secondly show $\lim_{n_{\text{steps}} \rightarrow \infty} S_{n_{\text{steps}}} \leq S^*$. Let $f \in \text{PC}^0([0, 1], \mathbb{R}^d)$. By definition of I_f ,

$$\forall \epsilon > 0, \exists n_{f,\epsilon} \in \mathbb{N} \text{ such that } \forall n \geq n_{f,\epsilon},$$

$$\left| \sum_{i=0}^{n-1} \frac{1}{P\left(\frac{f\left(\frac{i}{n}\right)+f\left(\frac{i+1}{n}\right)}{2}\right)} \left\| f\left(\frac{i+1}{n}\right) - f\left(\frac{i}{n}\right) \right\|_2 - I_f \right| \leq \epsilon.$$

Hence,

$$\forall \epsilon > 0, \exists n_{f,\epsilon} \in \mathbb{N} \text{ such that } S_{n_{f,\epsilon}} \leq I_f + \epsilon.$$

Moreover, since $\lim_{n_{\text{steps}} \rightarrow \infty} S_{n_{\text{steps}}} = \inf_{n_{\text{steps}} \geq 2} \{S_{n_{\text{steps}}}\}$, $\lim_{n_{\text{steps}} \rightarrow \infty} S_{n_{\text{steps}}} \leq I_f + \epsilon$ follows for any $\epsilon > 0$. Therefore, for any $f \in \text{PC}^0([0, 1], \mathbb{R}^d)$, $\lim_{n_{\text{steps}} \rightarrow \infty} S_{n_{\text{steps}}} \leq I_f$ holds. Therefore, we conclude that $\lim_{n_{\text{steps}} \rightarrow \infty} S_{n_{\text{steps}}} \leq S^*$. Finally we have

$$S_{n_{\text{steps}}} \xrightarrow{n_{\text{steps}} \rightarrow \infty} S^*.$$

□

Appendix B.2. Proof of Equation (2)

Proof. For the rest of the proof, we fix $n_{\text{steps}} \in \mathbb{N}$ such that $n_{\text{steps}} > 2$.

We firstly work at a fixed elementary event in the probability space where our random sequences are defined. Note that $\{S_{n_{\text{steps}}}^{(N)}\}_{N \geq 1}$ is lower bounded by 0 and non-increasing. Let $N \geq n_{\text{steps}}$. Since $\{z_j\}_{j=1}^N \subseteq \{z_j\}_{j=1}^{N+1}$, we have that $S_{n_{\text{steps}}}^{(N+1)} \leq S_{n_{\text{steps}}}^{(N)}$. Therefore, $\{S_{n_{\text{steps}}}^{(N)}\}_{N \geq 1}$ converges and its limit is

$$\lim_{N \rightarrow \infty} S_{n_{\text{steps}}}^{(N)} = \inf_{N \geq 2} \{S_{n_{\text{steps}}}^{(N)}\}.$$

We now have that $\{z_j\}_{j=1}^N \subseteq \mathbb{R}^d$ for every $N \geq 1$. This shows that for every realization of the random sequence

$$\forall N \geq 1 : S_{n_{\text{steps}}} \leq S_{n_{\text{steps}}}^{(N)}$$

and

$$S_{n_{\text{steps}}} \leq \lim_{N \rightarrow \infty} S_{n_{\text{steps}}}^{(N)}.$$

Let us consider the following function S defined as

$$S: (\mathbb{R}^d)^{n_{\text{steps}}-1} \longrightarrow \mathbb{R},$$

$$\{z_i\}_{i=1}^{n_{\text{steps}}-1} \longmapsto \sum_{i=0}^{n_{\text{steps}}-1} \frac{1}{P\left(\frac{z_i+z_{i+1}}{2}\right)} \|z_{i+1} - z_i\|_2.$$

We fix a discrete path $z = \{z_i\}_{i=1}^{n_{\text{steps}}-1} \subseteq \mathbb{R}^d$. As stated in Theorem 1, for any $i \in \{0, \dots, n_{\text{steps}} - 1\}$, $z_{i+1} \neq z_i$ and P is smooth. This means that S is also smooth in some open ball $B(z, \epsilon_z)$ centered at z with radius ϵ_z . Since S is smooth in $B(z, \epsilon_z)$, it is locally Lipschitz continuous in the closed ball $\bar{B}(z, \frac{\epsilon_z}{2})$ for some constant L_z . This comes from the mean value theorem and the fact that the gradient of S is bounded on the compact set $\bar{B}(z, \frac{\epsilon_z}{2})$.

Let $\epsilon > 0$. Then for any $z' \in \bar{B}(z, \frac{\epsilon_z}{2}) \cap \bar{B}(z, \frac{\epsilon}{L_z})$ we have

$$\begin{aligned} |S(z) - S(z')| &\leq L_z \|z - z'\|_2 \\ &\leq \epsilon. \end{aligned}$$

Furthermore, P is strictly positive almost everywhere. This means that with the notation $A_z = \bar{B}(z, \frac{\epsilon_z}{2}) \cap \bar{B}(z, \frac{\epsilon}{L_z})$,

$$\int_{A_z} P(v_1) \cdots P(v_{n_{\text{steps}}-1}) dv_1 \cdots dv_{n_{\text{steps}}-1} > 0$$

holds. Therefore, almost surely, there exists a rank N_z after which there exists $z' \in A_z$ such that $z' \subseteq \{z_j\}_{j=1}^{N_z}$. Then the following proposition holds:

$$\forall \epsilon > 0, \exists N_z \in \mathbb{N} \text{ almost surely such that } S_{n_{\text{steps}}}^{(N_z)} \leq S(z) + \epsilon,$$

which implies that $\lim_{N \rightarrow \infty} S_{n_{\text{steps}}}^{(N)} \leq S(z) + \epsilon$ for any $\epsilon > 0$ and in a subset of measure 1 of the probability space. Hence, we have $\lim_{N \rightarrow \infty} S_{n_{\text{steps}}}^{(N)} \leq S(z)$. We proved the inequality above for an arbitrary $z \in (\mathbb{R}^d)^{n_{\text{steps}}-1}$. We therefore have

$$\lim_{N \rightarrow \infty} S_{n_{\text{steps}}}^{(N)} \leq S_{n_{\text{steps}}}.$$

We finally have

$$S_{n_{\text{steps}}}^{(N)} \xrightarrow[N \rightarrow \infty]{a.s.} S_{n_{\text{steps}}}.$$

□

Appendix B.3. Proof of Lemma 1

Proof. Let A be a measurable set in \mathbb{R}^d . Then we have

$$\begin{aligned} \Pr(V \in g_\xi(A)) &= \Pr(z \in A) \\ &= \int_A P(z) d\mu \\ &= \int_{g_\xi(A)} P \circ g_\xi^{-1}(V) d\mu \circ g_\xi^{-1}. \end{aligned}$$

This property holds for all measurable sets A . Hence we conclude that $P_{\text{ed}} = P \circ g_\xi^{-1}$ by the definition of a probability density. □

Appendix B.4. Proof of Lemma 2

Proof. Set $A = \{g_\xi \circ f \mid f \in \text{PC}^0([0, 1], \mathbb{R}^d)\}$. Lemma 2 can be proved by showing $A = \text{PC}^0([0, 1], g_\xi(\mathbb{R}^d))$. We firstly prove $A \subseteq \text{PC}^0([0, 1], g_\xi(\mathbb{R}^d))$. Let $f \in \text{PC}^0([0, 1], \mathbb{R}^d)$. Since g_ξ is a topological embedding, then it is continuous on \mathbb{R}^d . Therefore, $g_\xi \circ f \in \text{PC}^0([0, 1], g_\xi(\mathbb{R}^d))$ as a composition of continuous and piecewise continuous functions.

We secondly prove $\text{PC}^0([0, 1], g_\xi(\mathbb{R}^d)) \subseteq A$. Let $g \in \text{PC}^0([0, 1], g_\xi(\mathbb{R}^d))$. Since g is valued in $g_\xi(\mathbb{R}^d)$, then $g_\xi^{-1} \circ g$ is well defined. As g_ξ is a topological embedding, g_ξ^{-1} is continuous on $g_\xi(\mathbb{R}^d)$ which leads $g_\xi^{-1} \circ g \in \text{PC}^0([0, 1], \mathbb{R}^d)$ as a composition of continuous and piecewise continuous functions. Furthermore, since $g = g_\xi \circ (g_\xi^{-1} \circ g)$, then consequently $g \in A$. Accordingly, we conclude that $A = \text{PC}^0([0, 1], g_\xi(\mathbb{R}^d))$. We also have and

$$\inf_{g \in \text{PC}^0([0, 1], g_\xi(\mathbb{R}^d))} \int_0^1 \frac{1}{P_{\text{ed}}(g(t))} dg(t) = \inf_{f \in \text{PC}^0([0, 1], \mathbb{R}^d)} \int_0^1 \frac{1}{P_{\text{ed}}(g_\xi \circ f(t))} dg_\xi \circ f(t)$$

by uniqueness of the infimum. □

Appendix B.5. Proof of Theorem 2

Proof. First, we prove the equation (3). Let $f \in \text{PC}^0([0, 1], \mathbb{R}^d)$. By the definition of piecewise continuous functions, there exists a family of compact subsets $\{[a_i, b_i]\}_{i \in I}$ of $[0, 1]$ such that I is finite and the restriction of f on each $[a_i, b_i]$ can be continuously extended into a continuous function $f_i: [a_i, b_i] \rightarrow \mathbb{R}^d$. We also have

$$\int_0^1 \frac{1}{P(f(t))} df(t) = \sum_{i \in I} \int_{a_i}^{b_i} \frac{1}{P(f_i(t))} df_i(t).$$

Since g_ξ is continuous, then $g_\xi \circ f_i$ is continuous for any $i \in I$, and we also have

$$\int_0^1 \frac{1}{P_{\text{ed}}(g_\xi \circ f(t))} dg_\xi \circ f(t) = \sum_{i \in I} \int_{a_i}^{b_i} \frac{1}{P_{\text{ed}}(g_\xi \circ f_i(t))} dg_\xi \circ f_i(t).$$

Let $i \in I$, then it holds that

$$\begin{aligned} & \int_{a_i}^{b_i} \frac{1}{P_{\text{ed}}(g_\xi \circ f_i(t))} dg_\xi \circ f_i(t) \\ &= \lim_{n \rightarrow \infty} \sum_{i=0}^{n-1} \frac{1}{P_{\text{ed}}(g_\xi \circ f_i \circ t_i(\frac{i}{n}))} \left\| g_\xi \circ f_i \circ t_i\left(\frac{i+1}{n}\right) - g_\xi \circ f_i \circ t_i\left(\frac{i}{n}\right) \right\|_2, \end{aligned} \tag{B.1}$$

where $t_i : x \mapsto a_i + (b_i - a_i)x$. We will refer to the final term in the equation B.1 as the Riemann sum.

Let $n \in \mathbb{N}$, f_i is continuous on a compact set $[a_i, b_i]$. By the Heine-Cantor theorem, it is therefore uniformly continuous on $[a_i, b_i]$. Therefore, $\exists \delta > 0$ such that

$$\forall i \in \{0, \dots, n-1\}, \left| t_i\left(\frac{i+1}{n}\right) - t_i\left(\frac{i}{n}\right) \right| \leq \delta \implies \left\| f_i \circ t_i\left(\frac{i+1}{n}\right) - f_i \circ t_i\left(\frac{i}{n}\right) \right\|_2 \leq \epsilon.$$

However, it holds that

$$\left| t_i\left(\frac{i+1}{n}\right) - t_i\left(\frac{i}{n}\right) \right| = \frac{b_i - a_i}{n},$$

and

$$\frac{b_i - a_i}{n} \xrightarrow{n \rightarrow \infty} 0.$$

The latter point means that

$$\exists N \in \mathbb{N}, \forall n \geq N, \frac{b_i - a_i}{n} \leq \delta.$$

Therefore, it holds that

$$\exists N \in \mathbb{N}, \forall n \geq N, \forall i \in \{0, \dots, n-1\}, \left\| f_i \circ t_i\left(\frac{i+1}{n}\right) - f_i \circ t_i\left(\frac{i}{n}\right) \right\|_2 \leq \epsilon,$$

which by the third assumption in Theorem 2 implies that

$$\exists N \in \mathbb{N}, \forall n \geq N, \forall i \in \{0, \dots, n-1\},$$

$$\left\| g_\xi \circ f_i \circ t_i \left(\frac{i+1}{n} \right) - g_\xi \circ f_i \circ t_i \left(\frac{i}{n} \right) \right\|_2 = C \cdot \left\| f_i \circ t_i \left(\frac{i+1}{n} \right) - f_i \circ t_i \left(\frac{i}{n} \right) \right\|_2.$$

Moreover, by the first assumption in Theorem 2 and Lemma 1, it holds that

$$P_{\text{ed}} \left(g_\xi \circ f_i \circ t_i \left(\frac{i}{n} \right) \right) = P \left(f_i \circ t_i \left(\frac{i}{n} \right) \right)$$

for any $n \in \mathbb{N}$ and any $i \in \{0, \dots, n-1\}$. By substituting these two equalities in the Riemann sum when n goes to infinity, we get

$$\int_{a_i}^{b_i} \frac{1}{P_{\text{ed}}(g_\xi \circ f_i(t))} dg_\xi \circ f_i(t) = C \cdot \int_{a_i}^{b_i} \frac{1}{P(f_i(t))} df_i(t).$$

Consequently, we obtain

$$\int_0^1 \frac{1}{P_{\text{ed}}(g_\xi \circ f(t))} dg_\xi \circ f(t) = C \cdot \int_0^1 \frac{1}{P(f(t))} df(t).$$

We then secondly prove the equation (4). By the second assumption in Theorem 2 and Lemma 2, we have

$$\inf_{g \in \text{PC}^0([0,1], g_\xi(\mathbb{R}^d))} \int_0^1 \frac{1}{P_{\text{ed}}(g(t))} dg(t) = \inf_{f \in \text{PC}^0([0,1], \mathbb{R}^d)} \int_0^1 \frac{1}{P_{\text{ed}}(g_\xi \circ f(t))} dg_\xi \circ f(t).$$

However, as we showed, we have

$$\int_0^1 \frac{1}{P_{\text{ed}}(g_\xi \circ f(t))} dg_\xi \circ f(t) = C \cdot \int_0^1 \frac{1}{P(f(t))} df(t).$$

for any $f \in \text{PC}^0([0,1], \mathbb{R}^d)$. Then, by property of the infimum we conclude that

$$\inf_{g \in \text{PC}^0([0,1], g_\xi(\mathbb{R}^d))} \int_0^1 \frac{1}{P_{\text{ed}}(g(t))} dg(t) = C \cdot \inf_{f \in \text{PC}^0([0,1], \mathbb{R}^d)} \int_0^1 \frac{1}{P(f(t))} df(t).$$

In other words,

$$S_{g_\xi(\mathbb{R}^d)}^* = C \cdot S_{\mathbb{R}^d}^*.$$

□